Journal of Alloys and Compounds 746 (2018) 370–376

Contents lists available at ScienceDirect

Journal of Alloys and Compounds

journal homepage: http://www.elsevier.com/locate/jalcom

The influence of nitrogen pressure on formation of niobium nitride by thermal processing

Ashraf Hassan Farha [a, d, 1], Osman Murat Ozkendir [b], Hani E. Elsayed-Ali [a], Suleyman Cabuk [c], Yuksel Ufuktepe [c, *]

[a] Department of Electrical and Computer Engineering and the Applied Research Center, Old Dominion University, Norfolk, VA, 23529, USA
[b] Tarsus Technology Faculty, Mersin University, Tarsus, 33480, Turkey
[c] Department of Physics, Cukurova University, Adana, 01330, Turkey
[d] Department of Physics, Faculty of Science, Ain Shams University, Cairo, 11566, Egypt

ARTICLE INFO

Article history:
Received 30 November 2017
Received in revised form
16 February 2018
Accepted 26 February 2018
Available online 6 March 2018

Keywords:
NbN_x
Nitride
Surface morphology
XRD
Thermal diffusion
X-ray absorption spectroscopy

ABSTRACT

The nitridation of niobium by thermal processing at 1300 °C in different nitrogen (N_2) gas pressures ranging from 2.6×10^{-4} to 3.3×10^{0} Pa was investigated. The NbN_x films were grown on the niobium substrate by reactive thermal heating. The effect of nitrogen background pressure on the structure and morphology of the formed NbN_x phase was studied by X-ray diffraction (XRD) and atomic force microscopy (AFM). The electronic structure of the NbN_x films was investigated by X-ray absorption near edge structure (XANES). The phase formation followed a sequence of α-Nb(N)→ β-Nb_2N when the nitrogen pressure was increased. As the pressure was increased to $>1.3 \times 10^{-3}$ Pa, the nitride film develop into the α-Nb(N) phase mixed with the β-Nb_2N phase. Increasing nitrogen pressure results in more β-phase concentration accompanied by an increase of other phases. Higher pressure promotes the diffusion of adsorbed nitrogen, and consequently the formation of different phases of NbN_x. The diffusion of nitrogen in the Nb surface and its reactivity governs the phase formation of NbN_x. XANES measurements at the Nb M-edge showed strong hybridizations between the Nb 4*d* and N 2*p* states due to larger covalent contribution to the Nb—N bonding. On the basis of these observations our density of state calculation revealed that presence of the β-Nb_2N phase in NbN_x results in a large covalent contribution than that by the α-NbN phase.

1. Introduction

Transition metal nitrides possesses an unusual combination of electronic and mechanical properties, which make them attractive for technological applications. In recent years, significant attention has been paid to the study of niobium nitride (NbN_x), which exhibits unique properties that makes it attractive for many technical and industrial applications. For instance, niobium nitride has high hardness and wear resistance, high superconducting transition temperature (T_c), and excellent thermal and chemical stabilities [1–4]. Niobium nitride thin films are of interest as they can be used for gas sensors, diffusion barriers in Josephson junctions, cathode materials in vacuum microelectronic devices, and coatings for superconducting cables [5–7]. NbN_x coatings on Nb show an increase in the surface hardness as well as they provide a barrier layer for the hydrogen diffusion into Nb for applications in superconducting radiofrequency cavities. NbN_x crystallize in different phases, including β-Nb_2N (hexagonal), γ-Nb_4N_3 (tetragonal) δ-NbN (face-centered cubic), δ′-NbN (hexagonal), ε-NbN (hexagonal), and the η-NbN (hexagonal) structure. The diffusion of nitrogen onto the niobium surface occurs by heating a niobium substrate at high temperatures in a background of nitrogen gas. Reactions between the diffused nitrogen with niobium occurs forming nitrides [8–12]. Combustion synthesis is another method used to form NbN_x [13]. NbN_x thin films were also produced by rapid thermal processing of Nb thin films, deposited on Si, in a background of molecular nitrogen or ammonia [14,15]. In general, these methods depend on adsorption of nitrogen or ammonia on the surface of niobium that is heated at high temperatures. Treatment of Nb samples at different heating temperatures or background pressures results in

* Corresponding author.
E-mail address: ufuk@cu.edu.tr (Y. Ufuktepe).
[1] A. H. Farha current address is Physics Department, College of Science, King Faisal University, Al Ahsa, 31982, Saudi Arabia.

https://doi.org/10.1016/j.jallcom.2018.02.304
0925-8388/

the formation of different NbN_x phases, stoichiometry, and morphology. The reactive diffusion process for NbN_x formation is simple, cheap, and results in uniformly covering larger areas with a homogenous thickness, and is effective in rapid formation of micron-size nitride layers [10,16]. NbN has a critical superconducting transition temperature (T_c) higher than Nb, it is very stable to structural disorder and radiation damage. The phase diagram of the Nb–N system is complicated and includes many different phases [17]. The selection of nitrogen background pressure and substrate temperature affects the phase of the NbN_x coating. Musenich et al., studied the nitride formation in 150 kPa N_2 background pressure in the temperature range 1100–1900 °C [10]. They observed formation of multiphases of NbN_x. Their work mainly focused on the growth kinetics and the mechanism of the reaction between the N_2 gas and Nb. That work, however, did not study the electronic structure of the NbN_x surface layer. We have previously studied NbN_x coatings formed by heating in the range of 1250–1500 °C at 1.3×10^{-3} Pa N_2 background gas pressure [16]. Only the α-NbN phase was detected with no transformation to another NbN_x phases observed. In the present study, we performed a series of experiments to investigate the formation of NbN_x in different background nitrogen gas pressures in the range 2.6×10^{-4} - 3.3×10^{0} Pa when heating Nb at 1300 °C. The study focuses on the structural and electronic characterization of NbN_x films formed with various nitrogen background pressures. The effect of the nitrogen gas pressure on the NbN_x phase formed is studied and conditions for the formation of the hexagonal β-Nb_2N phase, which is the hardest of the NbN_x phases [18], are identified.

2. Materials and methods

An ingot Nb substrate of 99.99% purity with dimensions of $8 \times 3 \times 0.2$ mm^3 was used. The substrate was mounted on a tungsten sample holder, which can resistively heat the sample up to 1500 °C. Standard buffered chemical polishing (BCP) method was used for cleaning the Nb substrate. The substrate was mounded in an ultrahigh vacuum (UHV) chamber pumped by a turbomolecular pump and an ion pump to a background pressure in the low 1.3×10^{-4} Pa. The Nb substrate was kept at 700 °C during the chamber bakeout. For nitridation, ultrahigh pure nitrogen (99.999%) was introduced into the chamber using a needle valve with the ion pump sealed and the chamber pumper by the 300 l/s turbomolecular pump. The thermal nitridation was done at different nitrogen background pressures ranging from 2.6×10^{-4} to 3.3 Pa at 1300 °C substrate temperature. The substrate temperature was measured using an optical pyrometer (IGA 15 plus, Mikron Infrared Inc.) through a quartz window and controlled by the current applied to the heater. The samples were processed for 180 min. In order to reach the desired pressure, the ion pump was turned off while the valve connecting the ultrahigh vacuum (UHV) chamber to the turbomolecular pump remained closed. Then, the ultrahigh purity nitrogen gas was introduced into the chamber through a variable leak valve to reach desired pressure. At the end of the 180 min nitridation process, the valve connecting the chamber to the turbomolecular pump was opened and the power to the sample heater was simultaneously turned off to allow the sample to cool down in vacuum after pump-down with the turbomolecular pump for 90 min. We used a different Nb substrate for each growth condition. The Nb substrates were all cleaned following the same BCP method.

XRD measurements were done using a Bruker-AXS three-circle diffractometer. The Bruker SMART APEX II instrument is equipped with graphite-monochromated CuK_α radiation and a SMART Apex II CCD detector. The X-ray source of wavelength 1.5406 Å ($CuK_{\alpha 1}$) is fixed and both the charge coupled device (CCD) detector 2θ and sample ω are movable. The detector 2θ is covering about 30° per image position. Three image positions were used for the experiment. In each case, the angle 2θ is the center position of the 30° CCD image, and each value is set so that the angles of incidence and diffraction are equal. Two dimensional (2D) XRD images are recorded for each sample.

The X-ray absorption near edge structure (XANES) measurements performed on beamline 8.2 at the Stanford Synchrotron Radiation Lightsource in the SLAC National Accelerator Laboratory. The beamline 8.2 is a bending-magnet beamline dedicated to photoemission, photoabsorption spectroscopy, and XANES experiments within an energy range of 100–1300 eV. The *M* edge spectra of niobum were measured in total electron yield (TEY) mode. The TEY signal in 3*d* transition metals is generated by secondary electrons following X-ray photon absorption. TEY spectra were collected at room temperature by measuring the sample current. The current measurements were done using a Stanford Research System low noise preamplifier Model SR570. The beam flux (I_o) signal from a gold grid was used to normalize the spectra. The X-ray incidence angle was controlled by a rotatable manipulator with an accuracy of about 0.2°. The base pressure of the chamber during the experiment was about 2.0×10^{-7} Pa.

3. Results and discussion

3.1. Structure and phase formation

Fig. 1 shows the XRD patterns of NbN_x films prepared by heating the Nb substrate at 1300° C in different nitrogen pressures for 180 min. The XRD pattern of the Nb substrate is also included in Fig. 1 as a reference.

Fig. 1 indicates that the films are polycrystalline and can be indexed based on the crystal structure of the bcc α-Nb(N) and the hexagonal β-Nb_2N phases [19,20]. The XRD data were fitted by the Material Analysis Using Diffraction (MAUD) program, for Rietveld analysis [21]. The crystal structures and lattice parameters were obtained using the MAUD software.

XRD peaks for samples prepared at 3.3 Pa showed β-Nb_2N mixed

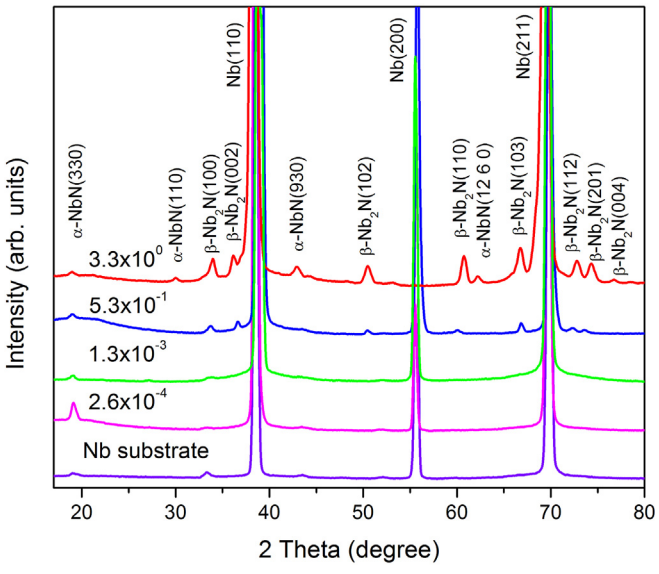

Fig. 1. XRD patterns of NbN_x thin films grown on Nb substrates at 1300° C temperature in different nitrogen background pressures. The nitrogen pressures in Pascals (Pa) are given at the side of each pattern. The XRD pattern of the Nb substrate is also shown at the bottom.

with other peaks attributed to α-Nb(N). The (100), (002), (102), (110), (103), (112), (201), and (004) peaks are attributed to the β-Nb_2N phase, while the (330), (110), (930), and (12 6 0) peaks are attributed to the α-Nb(N) phase. The formation of α-Nb(N) and β-Nb_2N phases agrees with the equilibrium phase diagram of NbN_x which predicts that the β-Nb_2N phase should appear in a temperature range that includes the presently used growth temperature of 1300 °C [22].

According to results by Zhitomirsky et al., when the surface of Nb was heated at high temperature, the α-Nb(N) forms followed by the β-Nb_2N phase [23]. This is also in agreement with what was previously reported on the reactivity of Nb in a nitrogen atmosphere in the same range of temperature [10]. The intensity of the peaks is enhanced as the nitrogen pressure is increased from 0.53 to 3.3 Pa, as observed from Fig. 1. The enhancement of peak intensity is due to increase of the samples thickness with background nitrogen pressure. The reactivity of the niobium surface with the nitrogen gas at high pressure is more effective than low pressure leading to the formation of the β-Nb_2N phase.

In the fitting process, the crystal lattice constants '*a*' and '*c*' were determined. The β-Nb_2N phase becomes dominant with the increase of nitrogen pressure. In order to see a more detailed picture of the crystal structure, we recorded the 2D-XRD images [24]. Fig. 2 shows 2D-XRD images of the samples that were heated at 1300 °C at different nitrogen pressures in the range of 2.6×10^{-4} to 3.3×10^{0} Pa. Mixed α and β phases start to be seen at a pressure of 1.3×10^{-3} Pa. The change in shape of the diffraction spots to continuous rings as the pressure increases is an indication of the formation of the β-Nb_2N phase crystallites.

For processing at a nitrogen pressure of 2.6×10^{-4} Pa, the shape of some diffraction spots of the Nb substrate is changed into continuous rings with uniform intensity, indicating the growth of small grains for heating athos relatively low N_2 pressure. Further increase of the nitrogen pressure causes the formation of larger grains, as can be seen by the spots in 2D XRD. With further increase in pressure, full spotty rings are obtained for the α and β phases, which indicated the formation of large grains on the surface with weak texture.

The crystallite size of the α-Nb(N) and β-Nb_2N phases was calculated from the XRD patterns by the Scherrer formula [25]:

$$D = \frac{0,9\lambda}{B\cos\theta}$$

where D is the crystallite size, λ is the x-ray wavelength (1.5406 Å), B is the full width half maximum of the XRD peak, and θ is the Bragg angle. Fig. 3 shows that the average crystallite size of the α-Nb(N) phase decreases from about 19.5 to 13.3 nm as the pressure of nitrogen is increased from 2.6×10^{-4} to 3.3 Pa. The error bars in Fig. 3 represent the standard deviations of the data. After the phase change, the crystallite size decrease in the bcc α-NbN phase could be due to compressive stress of the hexagonal β-Nb_2N phase.

The phase purity of the NbN_x films can be determined from the intensity of the XRD peaks. The average peak intensity for each phase was calculated from peak height and integrated area under each peak in Fig. 1. The β-Nb_2N phase concentration with change in nitrogen background pressure, shown in Fig. 4, is determined from the ratio of the sum of intensities of all the β-Nb_2N peaks divided by the total intensities of all peaks.

The lattice parameter of the β-Nb_2N phase was calculated from the peak positions in the XRD patterns, and shown in Table 1. We observe a large variation in the lattice parameters of the β-Nb_2N phase as the nitrogen gas pressure was increased (Fig. 4).

The error bars in Fig. 4 represent the standard deviation in

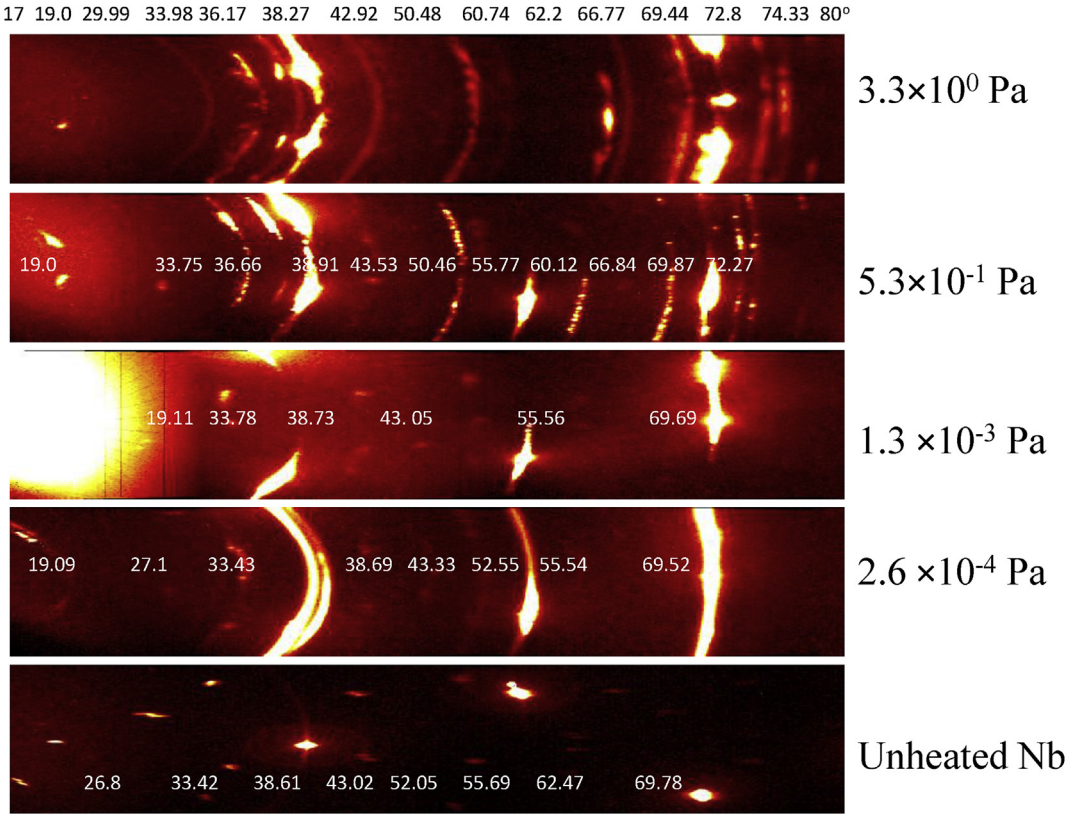

Fig. 2. 2D-XRD patterns of unheated Nb substrate and heat-treated Nb in different background nitrogen pressures for 180 min at 1300 °C.

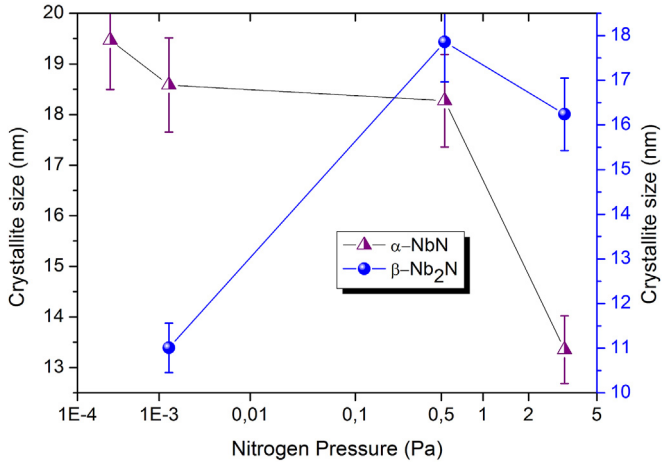

Fig. 3. Variation of crystallite size in NbNx films as a function of nitrogen gas pressure.

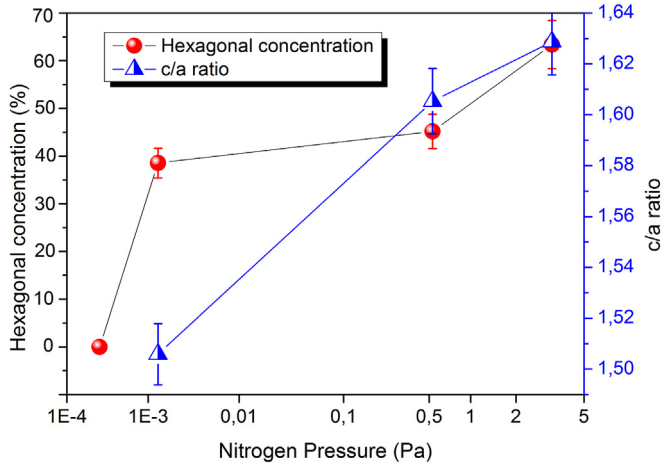

Fig. 4. Variation of the β-Nb_2N hexagonal phase concentration (left axis) and (c/a) ratio (right axis) of the β-Nb_2N phase with nitrogen background pressure.

Table 1
Calculated lattice parameters *a* and *c* for the β-Nb_2N phase depending on nitrogen pressure.

Nitrogen Pressure (*Pa*)	Calculated *c* value (*Å*)	Calculated n*a* value (*Å*)	Calculated *c*/*a* parameter (*Å*)
1.3×10^{-3}	4.6401	3.0811	1.5059
5.3×10^{-1}	4.8670	3.0318	1.6053
3.3×10^{0}	4.9674	3.0499	1.6287

calculating the hexagonal concentration and cell parameters from the XRD peaks of the same phase for different diffraction peaks. The unit cell parameter ratio (*c*/*a*) changes from 1.51 to 1.63. We note that the film deposited at 0.53 Pa nitrogen pressure has (*c*/*a*) ratio close to the bulk (1.619) value of β-Nb_2N. The β-Nb_2N phase has a distorted crystal structure at low gas pressures in the α-Nb(N) dominant NbN_x film but it reaches nearly bulk structure when the β-Nb_2N phase concentration is high.

Fig. 5(a–d) shows 3D AFM images of the NbN_x layer prepared at different nitrogen pressures at 1300 °C. The RMS surface roughness versus nitrogen pressure is plotted in Fig. 5(e). The RMS was obtained by performing line scans taken diagonally on the AFM images ($2 \times 2\ \mu m^2$). The error bars represent variations in RMS roughness in line scans from different AFM images with same area. The samples show a slight decrease in surface roughness as N_2 pressure increases, and the surface becames smooth as shown in Fig. 5 (d). As the pressure is increased to 3.3 Pa, some regularly-shaped islands start to form with increase of the β-Nb_2N phase.

32. XANES results

The total electron yield (TEY) detection is commonly used to record spectra of XANES, which is based on the measurement of drain current through the sample. The normalized Nb M-edge XANES signals of NbN_x samples heated at 1300 °C and different nitrogen pressures versus the photon energy are shown in Fig. 6(a). The spectra consists of two $3p_{3/2}$ and $3p_{1/2}$ doublets and a strong N 1*s* peak. The main features in the spectra are two maxima at 365.5, and 380.8 eV can be assign to the Nb $3p_{3/2}$ (M_3 edge) and $3p_{1/2}$ (M_2 edge), respectively. The Nb $M_{2,3}$ edges are attributed to the transition of Nb 3*p* electrons to unoccupied 4*d* and 5*s* states, where the spin-orbit coupling of the 3*p* electrons results in two sharp peaks. The peak at 365.5 eV is stronger than that at 380.8 eV due to the higher number of j = 3/2 states. The intensity of the N 1*s* peak at 406.6 eV is clearly seen in all samples but does not change with gas pressure. The detection of this N 1*s* peak by XANES confirms our observations on the formation of NbN_x in these samples.

The large spin-orbit interaction of the 3*p* core hole splits the XANES spectrum into M_3 ($3p_{3/2}$) and M_2 ($3p_{1/2}$) manifolds. The branching ratio (BR) gives the fraction of the total transition probability into the $3p_{3/2}$ level. The BR provides information on the valence band structure with spin orbit interaction. To estimate the experimental M_3–M_2 BR intensity, we used the normalized M_3 and M_2 peak heights as defined by:

$$\frac{I(M_3)}{[I(M_2) + I(M_3)]}$$

were $I(M_3)$ and $I(M_2)$ are the measured intensity of the peaks of j = 3/2 and j = 1/2 components, respectively. Fig. 6 (b) shows the measured BR as a function of the nitrogen pressure. It can be seen in Fig. 6 (b) that the BR increases significantly from 0.51 to 0.71 then decreased to 0.65 as pressure is increased. The origin of the observed BR increase with N_2 pressure can be explained in terms of both 3*p* and 4*d* levels of Nb. It was shown that an electrostatic interaction between the core electron and valence hole and the spin–orbit correlation of core electrons are affecting the BR [26]. This result reveals that the electron core–hole interaction between 3*p* and 4*d* levels increases with film thickness. The electronic structure changes a little for samples processed at 5.3×10^{-1} Pa pressure. The coordination of Nb and N atoms changes with increasing of the β-Nb_2N hexagonal phase concentration, which affects the electronic properties. With phase change from α-Nb(N) to β-Nb_2N, strong hybridizations between the Nb 4*d* and N 2*p* states occurs, suggesting larger covalent contribution to the Nb–N bonding. This indicates that samples processed at the higher pressure have a higher electron core hole interaction and number of 4*d* or 5*s* states available.

In order to better understand the electronic structure of NbN_x, we continue our analysis on these phases by calculating the α-Nb(N) and β-Nb_2N density of states (DOS) and partial density of states (PDOS) as shown in Fig. 7(a) and (b). Our plane-wave pseudopotential density functional theory calculations were carried out using the Vienna ab initio simulation package (VASP) [27] of the projector-augmented-wave method [28]. The pseudopotential employed in our calculations treat Nb $4p^6\ 4d^4\ 5s^1$ and N $2s^2\ 2p^3$ states as the valence states. The exchange-correlation energy is treated within the generalized gradient approximation as

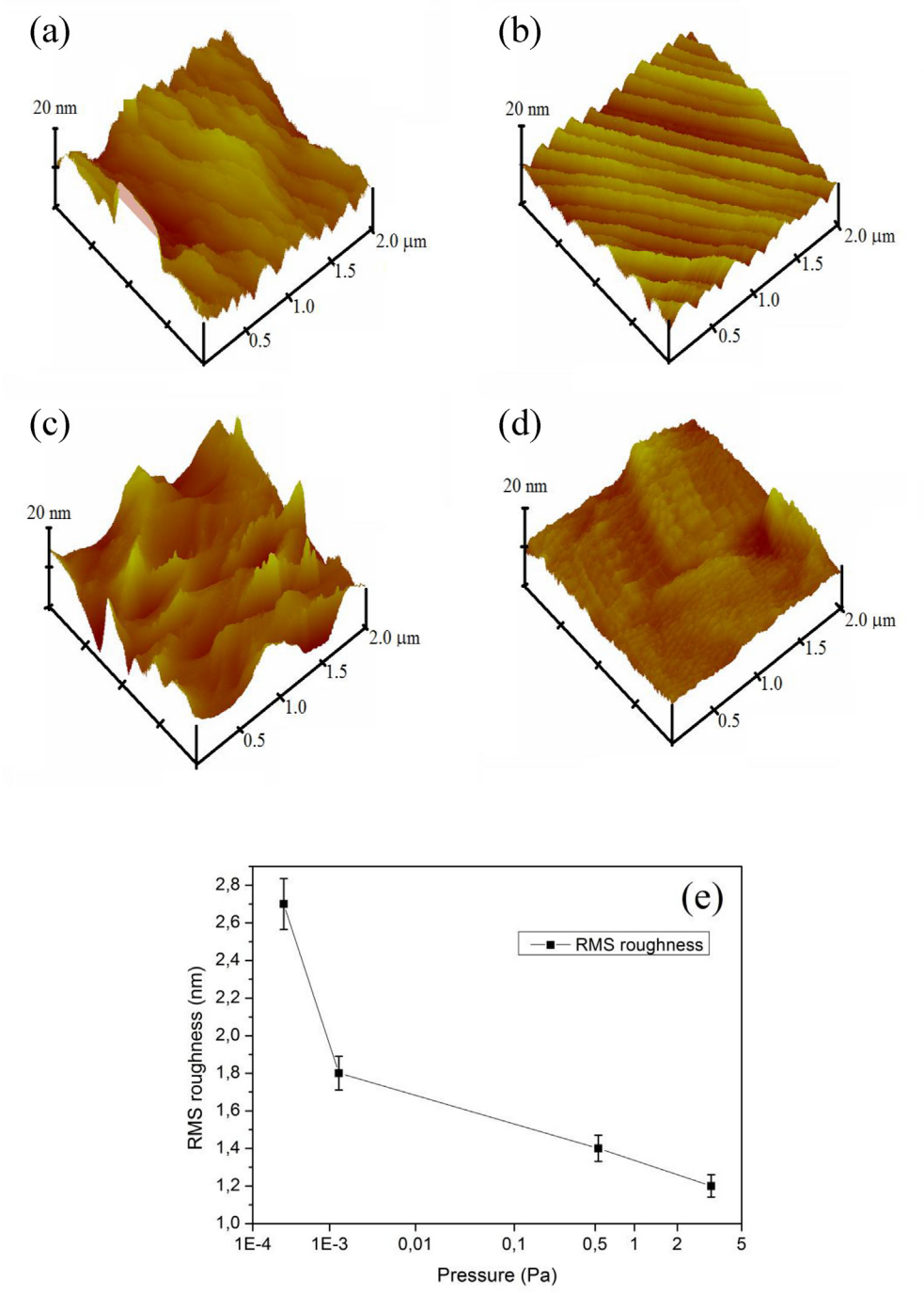

Fig. 5. 3D AFM images of NbN_x samples prepared for 180 min at 1300 °C in different nitrogen gas pressures; (a) 2.6×10^{-4}, (b) 1.3×10^{-3}, (c) 0.53, and (d) 3.3 Pa. (e) Dependence of surface roughness RMS values on nitrogen pressure.

parameterized by Perdew-Burke-Ernzerhof (PBE) scheme [29]. The Monkhorst-Pack method [30] with $12 \times 12 \times 12$ (α-NbN) and $12 \times 12 \times 10$ (β-Nb_2N) k-point meshes were used to sample the Brillouin zone. The plane-wave basis set with energy cut-off was set as 600 eV (α-NbN) and 750 eV (β-Nb_2N). The tetrahedron method [31] of Brillouin zone integration are used to compute the density of states. The equilibrium lattice constants are calculated from a structural optimization using conjugate gradient technique for both structures.

It is clear from Fig. 7 that the electronic structures of these two phases are different. The valence band mainly arises from hybridization between N-2*p* and Nb-4*d* states. The overlap of N-2*p* and Nb-4*d* levels is associated with the covalent bonding between niobium and nitrogen. The region just below and above the Fermi level originates from niobium 4*d* level. From Fig. 7 it appears that the energy region just above the Fermi energy is dominated by unoccupied Nb-4*d* states which shows higher DOS for the β-Nb_2N phase. Empty 4*d* states involve the excitation of 3*p* electrons into unoccupied *d*-orbital, the overall intensities of $M_{3,2}$ edge should depend on the density of the empty 4*d* state, so that the absorption process in XANES spectra can be described by the transition $4d^n \rightarrow 3p^5 4d^{n+1}$. It is likely that presence of the β-Nb_2N phase in

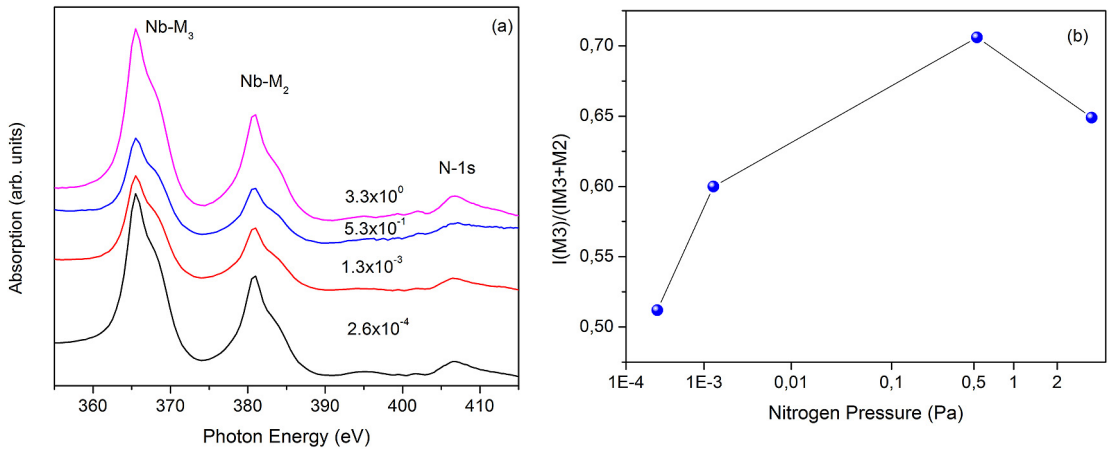

Fig. 6. (a) XANES spectra of NbN_x at the $M_{2,3}$ edge with varying working nitrogen pressures from 2.6×10^{-4} to 3.3 Pa in total electron yield (TEY) mode. (b) shows the branching ratio (BR) defined as the intensity-ratio I(M3)/[I(M2) + I(M3)] where I(M3) and I(M2) are the measured intensity of the peaks of j = 3/2 and j = 1/2 components, respectively.

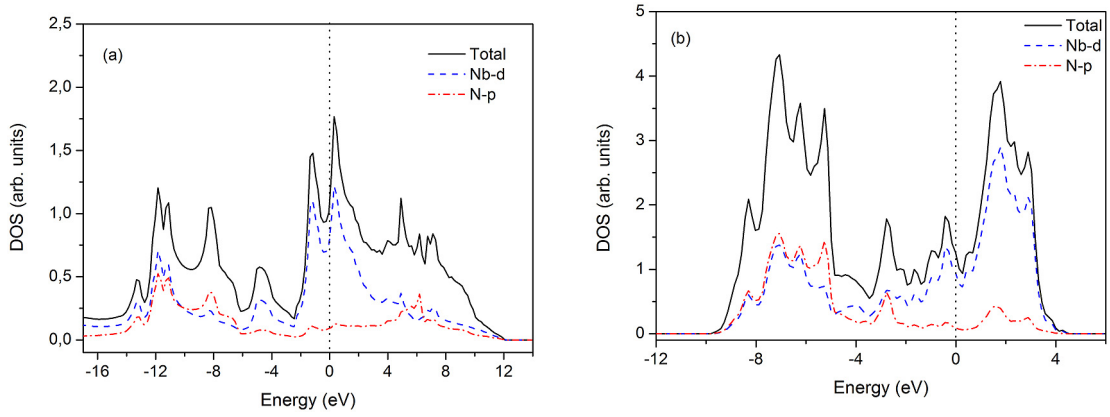

Fig. 7. Calculated partial and total density of states for (a) cubic α-Nb(N) and (b) hexagonal β-Nb_2N. Fermi levels are set to 0 eV.

NbN_x results a large covalent contribution than α-Nb(N) with higher number of 4*d* holes, which give rise to strong BR intensity.

4. Conclusion

Thermal diffusion of nitrogen under different nitrogen background pressures was studied. All samples were heated for 180 min. From XRD analysis, the formation of NbN_x with only α-NbN phase is observed at low nitrogen pressure. Then, the formed grains become smaller as nitrogen background pressure is increased. The reduced α-NbN grain size is calculated by the Scherrer relation. The average crystallite size of the α-Nb(N) phase decreases from about 19.5 to 13.3 nm when the pressure of N_2 is increased from 2.6×10^{-4} to 3.3 Pa. As pressure is increased to 1.3×10^{-3} Pa and higher, the NbN_x films consist of the α-Nb(N) phase mixed with the β-Nb_2N phase. The β-Nb_2N phase concentration and the ratio of the unit cell parameter ratio (*c*/*a*) increases with nitrogen pressure. The value of *c*/*a* changed from 1.51 to 1.63. The film deposited at 5.3 × 10-1 Pa nitrogen pressure has *c*/*a* ratio close to the bulk (1.619) value of β-Nb_2N. The 2D-XRD images show the formation α-Nb(N) phase grains at low N_2 pressures with the pattern showing ring shape indicative of small grains with lack of orientation. Further increase of the N_2 pressure during thermal processing results in larger grains. XANES measurements show a strong spin-orbit interaction resulting in a higher branching ratio at the *M*-edge due to increased number of *d*-holes in the samples. The BR increased significantly from 0.51 to 0.71 then decreased to 0.65 as the pressure is increased. This shows that the coordination of Nb and N atoms changes with increasing β-Nb_2N hexagonal phase concentration, which affects the electronic properties. From DOS calculations we see that N-2*p* states hybridize strongly with Nb-4*d* states and β-Nb_2N phase is more covalent than α-NbN phase.

Acknowledgments

A. H. F. was supported by a scholarship from the Egyptian Ministry of Higher Education and a Jefferson Lab scholarship funded by the Department of Energy Office of Nuclear Physics ARRA-NPQ project at Jefferson Lab under the U.S. DOE Contract No. DE-AC05-06OR23177. The authors are grateful to Stanford Synchrotron Radiation Light source (SSRL), California, USA, for providing the synchrotron-based XAS facility. Use of the SSRL source is supported by the US Department of Energy, Office of Basic Energy Sciences, under Contract No. DEAC02-76SF00515. Support of the DOE Cooperative Research Program for SESAME project is acknowledged by A.H.F., O.M.O. and Y.U. One of the authors (Y.U) acknowledge support from Cukurova University.

References

[1] S.T. Oyama, The Chemistry of Transition Metal Carbides and Nitrides, Blackie, London, 1996.
[2] J. Musil, Surf. Coating. Technol. 125 (2000) 322–330.

[3] L. Hultman, Vacuum 57 (2000) 1–30.
[4] X.-J. Chen, V.V. Struzhkin, Z. Wu, R.E. Cohen, S. Kung, H. Mao, R.J. Hemley, A.N. Christensen, Phys. Rev. B 72 (2005) 094514.
[5] Z. Wang, H. Terai, A. Kawakami, Y. Uzawa, Appl. Phys. Lett. 75 (1999) 701–703.
[6] M. Shcherbatenko, I. Tretyakov, Yu Lobanov, S.N. Maslennikov, N. Kaurova, M. Finkel, B. Voronov, G. Goltsman, T.M. Klapwijk, Appl. Phys. Lett. 109 (2016) 132602–132605.
[7] C.M. Natarajan, M.G. Tanner, R.H. Hadfield, Supercond. Sci. Technol. 25 (2012), 063001–0630016.
[8] H. Bauer, J. Low Temp. Phys. 24 (1976) 219–227.
[9] G. Brauer, J. Less Common Met. 2 (1960) 131–137.
[10] R. Musenich, P. Fabbricatore, G. Gemme, R. Parodi, M. Viviani, B. Zhang, V. Buscaglia, C. Bottino, J. Alloy. Comp. 209 (1994) 319–328.
[11] A.V. Linde, R.M. Marin-Ayral, D. Granier, F. Bosc-Rouessac, V.V. Grachev, Mater. Res. Bull. 44 (2009) 1025–1030.
[12] A.V. Linde, V.V. Grachev, R.M. Marin-Ayral, Chem. Eng. J. 155 (2009) 542–547.
[13] V. Buscaglia, F. Caracciolo, M. Ferretti, M. Minguzzi, R. Musenich, J. Alloy. Comp. 266 (1998) 201–206.
[14] C. Angelkort, H. Lewalter, P. Warbichler, F. Hofer, W. Bock, B.O. Kolbesen, Spectrochim. Acta, Part A 57 (2001) 2077–2089.
[15] A. Berendes, O. Brunkahl, C. Angelkort, W. Bock, F. Hofer, P. Warbichler, B.O. Kolbesen, Anal. Bioanal. Chem. 379 (2004) 554–567.
[16] A.H. Farha, O.M. Ozkendir, H.E. Elsayed-Ali, G. Myneni, Y. Ufuktepe, Surf. Coating. Technol. 309 (2017) 54–58.
[17] ASM, ASM Handbook: Volume 3: Alloy Phase Diagrams, ASM International, Materials Park, OH, 1992.
[18] M.A. Al Mamun, A.H. Farha, Y. Ufuktepe, H.E. Elsayed-Ali, A.A. Elmustafa, J. Mater. Res. 27 (2012) 1725–1731.
[19] I.C.f.D, Data, Powder Diffraction File 00-043-1420, 2004.
[20] I.C.f.D, Data, Powder Diffraction File 00-040-1274, 2004.
[21] L. Lutterotti, Nucl. Instrum. Methods Phys. Res., Sect. B 268 (2010) 334–340.
[22] W. Lengauer, M. Bohn, B. Wollein, K. Lisak, Acta Mater. 48 (2000) 2633–2638.
[23] V.N. Zhitomirsky, I. Grimberg, L. Rapoport, N.A. Travitzky, R.L. Boxman, S. Goldsmith, A. Raihel, I. Lapsker, B.Z. Weiss, Thin Solid Films 326 (1998) 134–142.
[24] B.B. He, Two-dimensional X-Ray Diffraction, Wiley-Interscience, Hoboken, USA, 2009.
[25] B.D. Cullity, Elements of X-ray Diffraction, Addison-Wesley, New York, 1956.
[26] F.M.F. de Groot, Physica B 208 & 209 (1995) 15.
[27] a) G. Kresse, J. Furthmuller, Comput. Mater. Sci. 6 (1996) 15;
b) G. Kresse, J. Furthmuller, Phys. Rev. B 54 (1996) 11169 (more info of computer code VASP. See, http://cms.mpi.univie.ac.at/vasp.
[28] a) P.E. Blöchl, Phys. Rev. B 50 (1994) 17953;
b) G. Kresse, D. Joubert, Phys. Rev. B 59 (1999) 1758.
[29] J.P. Perdew, S. Burke, M. Ernzerhof, Phys. Rev. Lett. 77 (1997) 3865–3868.
[30] J.H. Monkhorst, J.D. Pack, Phys. Rev. B 13 (1976) 5188–5192.
[31] P.E. Blöchl, O. Jepsen, O.K. Andersen, Phys. Rev. B 49 (1994) 16223–16232.